

# Contact Stability and Contact Safety of a Magnetic Resonance Imaging-Guided Robotic Catheter under Heart Surface Motion

**Ran Hao \***

Department of Electrical, Computer,  
and Systems Engineering Engineering  
Case Western Reserve University  
Cleveland, Ohio 44106  
Email: rxh349@case.edu

**E. Erdem Tuna**

Department of Electrical, Computer,  
and Systems Engineering Engineering  
Case Western Reserve University  
Cleveland, Ohio 44106  
Email: eet12@case.edu

**M. Cenk Çavuşoğlu**

Department of Electrical, Computer,  
and Systems Engineering Engineering  
Case Western Reserve University  
Cleveland, Ohio 44106  
Email: mcc14@case.edu

*Contact force quality is one of the most critical factors for safe and effective lesion formation during catheter based atrial fibrillation ablation procedures. In this paper, the contact stability and contact safety of a novel magnetic resonance imaging (MRI)-actuated robotic cardiac ablation catheter subject to surface motion disturbances are studied. First, a quasi-static contact force optimization algorithm which calculates the actuation needed to achieve a desired contact force at an instantaneous tissue surface configuration is introduced. This algorithm is then generalized using a least-squares formulation to optimize the contact stability and safety over a prediction horizon for a given estimated heart motion trajectory. Four contact force control schemes are proposed based on these algorithms. The first proposed force control scheme employs instantaneous heart position feedback. The second control scheme applies a constant actuation level using a quasi-periodic heart motion prediction. The third and the last contact force control schemes employ a generalized adaptive filter based heart motion prediction, where the former uses the predicted instantaneous position feedback, and the latter is a receding horizon controller. The performance of the proposed control schemes are compared and evaluated in a simulation environment.*

## 1 Introduction

Robotic catheter ablation technology has been proposed to improve treatment of atrial fibrillation [1–4] by providing the catheter with dexterous manipulation and precise navigation capabilities. A successful atrial fibrillation ablation procedure requires the physician to apply radiofrequency energy with the catheter to create gap-free transmural lesions in the left atrium to stop the abnormal electrical signals in the heart that cause the rhythm problems. In order to create a gap-free ablation lesion, the robotic catheter needs to maintain stable contact with the substrate tissue surface with appropriate contact force during the radiofrequency application.

Rapid heart motion is one of the major disturbances for cardiac ablation procedures, which can result in inaccurate lesion formation, potentially leading to incomplete treatment and recurrence of arrhythmia. Rapid heart beating motions make it difficult to keep adequate contact between the catheter tip and the tissue surface. Unstable contact between the catheter tip and the tissue surface increases the possibility of sliding and positional errors [4]. As suggested in [5], the cardiac motion causes the displacement of desired ablation target point up to 1 centimeter, leading to inadequate or excessive contact force on the tissue surface. As such, maintaining stable and safe contact while being subjected to the beating heart motions is critical. Therefore, enhancing contact stability has become the cornerstone for the development of catheter ablation technologies [6–8].

The aim of this paper is the development of methods for providing robust contact stability and maintaining safe contact force for a novel magnetically-actuated robotic intravascular cardiac catheter system. The MRI-actuated robotic

---

\*This work was supported in part by the National Science Foundation under grants CISE IIS-1524363, CISE IIS-1563805, ENG IIP-1700839, and the National Heart, Lung, and Blood Institute of the National Institutes of Health under grant R01 HL153034. This paper was presented in part at the 2020 IEEE International Conference on Robotics and Automation (ICRA 2020), Paris, France.

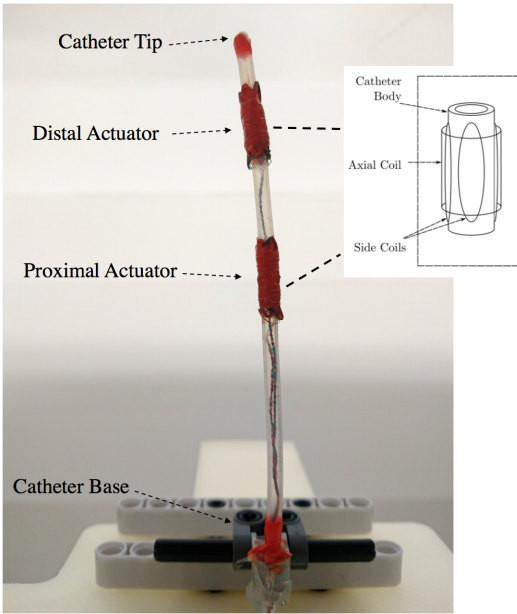


Fig. 1. The MRI-actuated catheter with two sets of actuation coils [9].

catheter, developed in [9–11], is equipped with two sets of current-carrying micro-coils and operated inside the bore of an MRI scanner to perform ablation, as shown in Fig. 1. Each set of coils (or actuators) contains one axial coil, and two orthogonal side coils [9]. The robotic catheter is actuated by the magnetic torque generated by the MRI scanner’s magnetic field on the coils [10, 12–14].

In this paper, the contact stability and contact safety of the MRI-actuated robotic catheter during heart motion are studied. Specifically, stable catheter-tissue contact guarantees no slippage between the catheter-tip and the tissue surface under the heart motion disturbances, and safe catheter-tissue contact ensures the normal contact force to remain within the desired force limits under the heart motion disturbances. First, the contact model for the pseudo-rigid-body model of the robotic catheter is introduced. The contact force-actuation Jacobian, which approximates the relationship between the changes of the contact force and the changes of the actuation currents, is then formulated. Two contact force optimization algorithms that use this Jacobian are then proposed. The first method is a quasi-static contact force optimization algorithm which iteratively calculates the actuation needed to achieve a desired contact force for an instantaneous surface configuration. The second method is a least-squares based contact force optimization algorithm which provides stable and safe contact forces against predicted heart motion trajectories over a given prediction horizon. In this method, the contact force residuals are minimized over the estimated heart motion trajectory provided by the heart motion prediction method. Four contact force control schemes are then proposed building on these contact force optimization algorithms to achieve safe and stable catheter-tissue contact under heart motion disturbances. Specifically, the first control scheme proposed is an instan-

taneous heart position feedback-based method. The second scheme applies a constant actuation level based on a quasi-periodic heart motion prediction. In [15–17], the experimental analysis has shown that the generalized adaptive filter-based heart motion prediction was able to provide the estimated motion trajectories with high accuracy and better robustness for heart motion tracking problems under both regular and arrhythmia heart motions, compared with other state-of-the-art motion prediction methods. In the third contact force control scheme, a prediction feedback based method employing the generalized adaptive filter-based heart motion prediction [16] is proposed. The same heart motion prediction method is then employed in a receding horizon controller in the last contact force control scheme proposed. The effectiveness and robustness of the proposed contact force control schemes are evaluated in a simulation environment using prerecorded *in vivo* heart motion data.

The rest of this paper is organized as follows. Related studies in the literature are presented in Section 2. The pseudo-rigid-body (PRB) model of the MRI-actuated robotic catheter is reviewed and presented in Section 3. The catheter-tissue contact model based on the PRB model is then provided in 4. The contact force control schemes are presented in Section 5. The contact stability and safety analysis and simulation-based validations of the contact force control schemes are presented in Section 6. Finally, discussions and conclusions are presented in Section 7 and 8, respectively.

## 2 Related Work

Several studies have shown that contact force plays a critical role in lesion formation during catheter ablation [18–22]. Adequate contact force is required to transfer the heat energy from the catheter tip to the target tissue surface for an effective lesion formation [20, 23]. Low contact force may cause failure of tissue heating and transient lesion formation, increasing the risk of recurrence of arrhythmia [8]. Excessive contact force can lead to severe complications, including steam pop, thrombus formation, and perforation [6].

Force-sensing radiofrequency ablation catheters have been investigated in several studies in order to better assess the relationship between contact force and ablation efficacy [6–8, 18]. Reddy et al. study the relationship between contact force and clinical recurrences for pulmonary vein isolation (PVI) using a contact force ablation system [20]. This study shows that the contact force for achieving clinical efficacy in PVI should be  $> 10$  g (0.1 N), and arrhythmia is best controlled with contact force  $> 20$  g (0.2 N). In [22], Wakili et al. show that all patients treated with contact force  $< 10$  g experienced arrhythmia recurrence. Similarly, Andrade et al. [24] show that low contact force  $< 10$  g is associated with higher rate of arrhythmia recurrence (100%) compared to contact force  $> 20$  g (20%). Williams et al. [19] suggest that high contact force  $> 25$  g may result in heating and edema of extracardiac structures. In this study, we restrict the desired normal contact force range from 10 g to 25 g (0.1 N~0.25 N), and investigate the ability of the MRI-actuated robotic catheter to maintain the contact force in this narrow thera-

peutic range during the heart motion [5].

In [8, 19, 25], it has been shown that contact stability is essential for safety and long-term efficacy of atrial fibrillation ablation. Dewire and Calkins [25] propose that advanced technologies, including contact force sensing catheters and MRI-guided catheters, are promising to improve the success rate and safety of ablation. In [26], Biase et al. show that using a remote robotic manipulation system can improve the efficacy and safety of ablation procedures. Jayender et al. [27] present an image guided active robotic catheter with shape memory alloy actuators, using a closed-loop PID controller to regulate the tip position and force with additional sensors. Srimathveeravalli et al. [28] design a teleoperated endovascular robotic system for achieving better performance on positioning and force control. Yuen et al. [29] developed a motion compensation system for contact force control under the beating heart motions. Kesner et al. [4] propose a 3D ultrasound image guidance based robotic catheter system with a force sensing end-effector in order to keep a constant contact force against the tissue motion. Yip et al. [30] develop an adaptive Jacobian estimation method for closed-loop position control of a catheter under heart motion disturbances, where a force sensor is employed to regulate the contact force. Several sensor-less contact force estimation methods, employing pose measurement or distal shaft measurement based on different kinematic models of the catheter, are proposed in [31–33]. Razban et al. [34] propose an approach estimating multiple contact point forces using contact point tracking and image-based deflection measurement. In [35], a closed-loop controller is designed based on finite element model of the catheter, where the contact force, modeled by Signorini’s contact model, is solved numerically as a constrained optimization problem. Haouchine et al. [36] propose an approach that compute contact force using only visual feedback from stereoscopic camera.

While many studies have proposed the strategies to achieve safe robot-tissue contact for robotic catheters [4, 29, 30], maintaining a stable robot-tissue contact with a safe contact force for the robotic catheter under the beating heart motions remains a challenge. In this paper, we present the analysis of the contact stability and contact safety of the MRI-actuated robotic catheter under cardiac tissue motions. Specifically, we investigate how to control the contact force for maintaining a stable and safe catheter-tissue contact under heart motion disturbances. Unlike the above studies, the proposed contact force control methods are formulated based on the calculation of the contact force-actuation Jacobian without using additional force sensors.

In our previous work presented in [37], the proposed least-squares based contact control scheme is implemented employing a simple heart motion prediction method, which uses the first cycle of the heart motion as the prediction of the subsequent heart beat motions. However, the robustness of the contact force control method cannot be guaranteed when dealing with large temporal variance of the heart motion. In this paper, two force control methods which employ recursive least-squares adaptive filter based heart motion prediction, are presented. Additionally, in [37], the con-

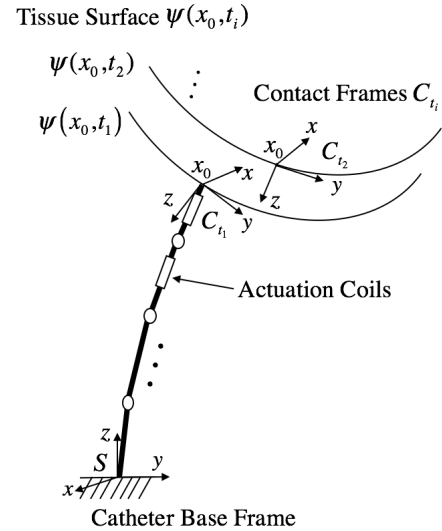


Fig. 2. The PRB model of the MRI-actuated robotic catheter with two actuators under surface contact constraint. Each actuator contains one set of tri-axial actuation coils. The contact frame  $C$  is chosen such that its origin is located at the contact point of the catheter and the  $z$ -axis is the outward normal of the tissue surface.  $x_0$  denotes the contact point position in surface frame, which remains static during heart surface motion.  $\Psi(x_0, t_i)$  denotes the parametrization of tissue surface given contact point  $x_0$  at time  $t_i$ .  $S$  denotes the spatial frame of the catheter.

tact force control methods are implemented assuming zero time lag between the MRI image acquisition for measurement of the heart motion and the control update. However, such an assumption cannot be applied to the MRI-guided robotic catheter in practice because of the time needed for MRI image acquisition, construction, and processing. In the present paper, an investigation of how the proposed contact force control schemes perform under different time lags between the measurement and the control update is presented. As such, the validation studies and discussion of the results are updated and expanded in the present paper compared to [37]. Additionally, a more extensive literature review is presented.

### 3 Pseudo-Rigid-Body Model of the Catheter

The kinematic models of the MRI-actuated robotic catheter are provided in [10] and [38], including the continuum model based on finite differences approach and beam theory, and the pseudo-rigid-body model (PRBM), respectively. The continuum model of the robotic catheter is able to describe the catheter deflection with high reproducibility and accuracy [39], but with low computation efficiency. In this paper, the pseudo-rigid-body model is employed as the kinematic model of the robotic catheter due to its computational efficiency.

Pseudo-Rigid-Body (PRB) model approximates the catheter as a series of pseudo-rigid links connected by elastic joints [38, 40–42], as shown in Fig. 2. Each joint is modeled

as a spherical joint which is parametrized by three rotation angles in a set of axis-angle representations [43]. The rotation angle of the  $i$ -th joint is given as  $\theta_i = [\theta_{ix}, \theta_{iy}, \theta_{iz}]^T$ , which assumes non-ordered rotations. The twist of the  $i$ -th joint is given as

$$\xi_i(\theta_i) = \begin{bmatrix} -\theta_i \times q_i \\ \theta_i \end{bmatrix}, \quad (1)$$

where  $q_i$  is the initial position of the  $i$ -th joint in spatial frame. And the forward kinematics of the catheter is then given as [44]:

$$g_{st}(\theta) = e^{\hat{\xi}_1 \theta_1} e^{\hat{\xi}_2 \theta_2} \dots e^{\hat{\xi}_n \theta_n} g_{st}(0), \quad (2)$$

where  $g_{st}(0)$  is the initial configuration,  $S$  denotes the spatial frame, and  $T$  denotes catheter tip frame. The shape of the catheter under the  $n+1$ -link PRB model can then be described by the joint angle vector  $\theta = [\theta_1^T, \theta_2^T, \dots, \theta_n^T]^T \in \mathcal{C} \subset \mathbb{R}^{3n}$ , where  $\mathcal{C}$  denotes the configuration space of the robotic catheter [43].

The magnetic moment  $\mu_j$  generated by the  $j$ -th actuator embedded on the catheter with currents  $u_j \in \mathbb{R}^3$  is computed as  $n_j A_j u_j$ , where  $j = 1, \dots, M$ , and  $M$  is the number of actuators.  $n_j$  and  $A_j$  are 3 by 3 diagonal matrices whose diagonal elements are the number of winding turns and the cross sectional areas (in body frame) of the micro-coils in the tri-axial actuation coil set of the actuator  $j$ , respectively. The static magnetic field  $B_s$  of the MRI scanner expressed in the body frame of the  $j$ -th actuator is given as  $B_j = R_{sj}^T B_s$ , where  $R_{sj}^T$  denotes the rotation matrix of the frame attached to the  $j$ -th actuator relative to the spatial frame [9]. The resulting Lorentz forces generated on the coils by the static magnetic field is given by  $(n_j A_j u_j) \wedge B_j = -B_j \wedge (n_j A_j) u_j$ , where  $\wedge$  is the cross product operator.

These actuation moments can then be mapped to the joint torques  $\tau(\theta, u) \in \mathbb{R}^{3n}$  as [43]:

$$\tau(\theta, u) = \sum_j^M J_{su_j}^b{}^T \begin{bmatrix} 0 \\ B_j \wedge (n_j A_j) \end{bmatrix} u_j = A(\theta) u. \quad (3)$$

Here,  $J_{su_j}^b$  is the body Jacobian corresponding to actuator  $j$ , and

$$A(\theta) = \begin{bmatrix} \dots & J_{su_j}^b{}^T \begin{bmatrix} 0 \\ B_j \wedge (n_j A_j) \end{bmatrix} & \dots \end{bmatrix}, \quad (4)$$

$j = 1, \dots, M$ .  $\tau(\theta, u)$  will be denoted as  $\tau_u$  in the rest of the paper for convenience.

## 4 Contact Model of the MRI-actuated Robotic Catheter

### 4.1 Contact Force and Contact Ratio

The contact force model, and the contact ratio as a measure of the contact stability are introduced in this section.

The friction cone for the contact is defined as:

$$FC = \{f_c \in \mathbb{R}^3 : \sqrt{\lambda_{f1}^2 + \lambda_{f2}^2} \leq \mu_s \lambda_c\}, \quad (5)$$

where  $f_c$  denotes the contact force,  $\mu_s$  denotes the static friction coefficient.  $\lambda_c$ ,  $\lambda_{f1}$  and  $\lambda_{f2}$  respectively denote the normal and the two tangential components of the contact force. The set of contact forces which cause no slippage between the tip and the surface must lie in the friction cone. Suppose the contact between catheter and the surface is non-conforming, the origin of the contact frame is located at the contact point, and its z-axis is in the outward surface normal direction (Fig. 2). Then the contact force would be in the form  $f_c = [\lambda_{f1}, \lambda_{f2}, \lambda_c]$ . The associated contact Jacobian  $J_C \in \mathbb{R}^{3 \times 3n}$  relating contact forces to joint torques [45] is given by:

$$J_C = \mathbf{B}_c^T \text{Ad}_{g_{sc}^{-1}} J_{st}^s, \quad (6)$$

$$\text{Ad}_{g_{sc}^{-1}} = \begin{bmatrix} R_{sc}^T & -R_{sc}^T p_{sc} \\ 0 & R_{sc}^T \end{bmatrix}, \quad (7)$$

where the wrench basis  $\mathbf{B}_c = [I^{3 \times 3}, 0^{3 \times 3}]^T$ ,  $J_{st}^s$  denotes the spatial manipulator Jacobian of the catheter.  $g_{sc}$  denotes the transformation from the contact frame to the spatial frame, and,  $R_{sc}$  and  $p_{sc}$  are respectively the rotational and translational components of the contact frame to spatial frame transformation.

The quasi-static equilibrium<sup>1</sup> equation of the catheter describing the relationship between the catheter shape and the actuation currents under the tip contact position constraint is given by:

$$N(\theta) + K\theta - J_C^T f_c - \tau_u = 0, \quad (8)$$

where  $K$  is the stiffness coefficient matrix, and  $N$  is the gravitational effect term. The contact force is then calculated as:

$$f_c = J_C^{T\dagger} (N(\theta) + K\theta - \tau_u), \quad (9)$$

where  $J_C^{T\dagger}$  is the left pseudo-inverse of  $J_C^T$  with  $J_C^{T\dagger} = (J_C J_C^T)^{-1} J_C^T$ .

The contact ratio  $\sigma_\mu$  between friction force and normal force is defined as:

$$\sigma_\mu(\theta, u) = \frac{\|\lambda_f\|}{\lambda_c}, \quad (10)$$

where  $\sigma_\mu \in \mathbb{R}$ . The catheter tip remains on the target contact point if the contact force is inside the friction cone  $FC$ , or equivalently,  $0 \leq \sigma_\mu \leq \mu_s$ , where  $\mu_s$  is the static friction coefficient between the catheter tip and the tissue surface.

<sup>1</sup>Since the catheter moves with low velocity and acceleration during catheter ablation, the inertial and Coriolis forces are negligible, and therefore can be neglected.

## 4.2 Contact Force-Actuation Jacobian

In this section, contact force-actuation Jacobian is derived to approximate the relationship between the changes in contact forces and the changes in actuation currents.

Substituting (3) into the quasi-static equilibrium equation (8) as

$$J_C^T f_c = N(\theta) + K\theta - A(\theta)u. \quad (11)$$

At a given joint configuration  $\theta_0$ ,  $A(\theta)$  and  $N(\theta)$  can then be approximated at  $\theta_0$  using Taylor's theorem as  $A(\theta) \approx A(\theta_0) + A'(\theta_0)\Delta\theta$  and  $N(\theta) \approx N(\theta_0) + N'(\theta_0)\Delta\theta$ , where  $A'(\theta_0) = \partial A/\partial\theta|_{\theta=\theta_0}$ <sup>2</sup> and  $N'(\theta_0) = \partial N/\partial\theta|_{\theta=\theta_0}$ . Then (11) can be linearized as

$$J_C^T f_c \approx (N(\theta_0) + N'(\theta_0)\Delta\theta) + K\theta_0 - (A(\theta_0) + A'(\theta_0)\Delta\theta)u. \quad (12)$$

Since the joint displacement  $\Delta\theta$  is small based on the quasi-static assumption, (12) can be approximated as

$$J_C^T f_c \approx N(\theta_0) + K\theta_0 - A(\theta_0)u. \quad (13)$$

The contact force-actuation Jacobian  $J_{cu}$  at joint configuration  $\theta_0$  is then calculated as

$$J_{cu} = df_c/du \approx -J_C^{T\dagger} A(\theta_0). \quad (14)$$

## 5 Contact Force Control Under Surface Motion

Let  $\Psi(x, t)$  denote the parametrization of the tissue surface,  $x = x_0$  be the location of the desired contact point in surface frame, and  $t$  denote the time. Let  $h(\theta)$  denote the forward kinematics of the catheter, and  $h: \mathbb{R}^{3n} \rightarrow \mathbb{R}^3$ . As shown in Fig. 2, during heart surface motion, catheter tip position is required to be static in the surface frame, i.e.  $h(\theta_t) = \Psi(x_0, t)$ . The goal of the contact force control is to improve the stability and safety of the catheter tip-tissue surface contact under surface motion, namely, maintaining static catheter tip positioning at the desired location on the tissue surface with appropriate normal contact force, despite heart motion.

In this section, we first introduce a quasi-static contact force optimization algorithm, which computes a set of actuation currents for a desired normal contact force and target tip position under a given instantaneous surface configuration. This algorithm is then generalized using a least squares formulation to optimize the contact stability and safety for a given estimated heart motion trajectory over a prediction horizon. Four contact force control schemes are then proposed based on these algorithms.

---

### Algorithm 1: Quasi-Static Contact Force Optimization with Tip Position Constraint for Robotic Catheter

---

**Input** :  $u^0, f_{cn}^d, \Psi(x_0)$   
**1**  $t \leftarrow 0$   
**2** **while**  $|f_{cn}^d - f_{cn}^t| > \epsilon$  **do**  
**3**      $\theta^t \leftarrow \text{constrained\_equilibrium}(u^t, \Psi(x_0))$   
**4**      $f_c^t \leftarrow \text{compute\_contact\_force}(\theta^t, u^t, \Psi(x_0))$   
**5**      $df_c^n \leftarrow k_n(f_{cn}^d - f_{cn}^t)$   
**6**      $df_c^t \leftarrow (-k_f f_{cx}^t, -k_f f_{cy}^t, df_c^n)$   
**7**      $J_{cu} \leftarrow -J_C^{T\dagger} A(\theta^t)$   
**8**      $du \leftarrow J_{cu}^{\dagger} df_c^t$   
**9**      $u^{t+1} \leftarrow u^t + du$   
**10**     $t \leftarrow t + 1$   
**11** **end**  
**Output**:  $u^t$

---

## 5.1 Quasi-Static Contact Force Optimization Algorithm

Under a given instantaneous surface configuration, the proposed quasi-static contact force optimization algorithm iteratively computes the actuation currents to achieve a desired normal contact force and target tip position, as presented in Algorithm 1.

The algorithm assumes that the catheter tip is initially in contact with the target point position on the tissue surface. The initial actuation current  $u^0$ , the desired normal contact force  $f_{cn}^d$ , and the spatial coordinates of the contact point on the tissue surface  $\Psi(x_0)$  are given as inputs. In this algorithm, because the contact force is controlled for a given instantaneous configuration of the surface (hence the name quasi-static), the time parametrization  $t$  in  $\Psi(x_0, t)$  is excluded. In Line 3, the quasi-static equilibrium configuration of the catheter is computed for the given input currents and the tissue surface contact point. In this step, a potential energy minimization based algorithm is performed in the constrained space in order to guarantee the tip position constraint [9, 44]. The contact force  $f_c$  is then updated given the updated joint angles and actuation currents using (9). The incremental change of the normal contact force  $df_c^n$  is then calculated from the desired normal component of the contact force in Line 5, where  $k_n$  is the step size to adjust the update speed. The incremental change of the contact force  $df_c$  is calculated in Line 6. A negative feedback  $-k_f$  is applied on the tangential forces to keep the contact force inside the friction cone during the contact control, while the normal component is driven towards the desired value. In line 7, the contact force-actuation Jacobian  $J_{cu}$  is computed given current joint configuration using (14). The incremental current update  $du$  is computed and applied respectively in Lines 8 and 9. The algorithm returns the resulting actuation currents once the desired normal force is achieved.

<sup>2</sup>Note that  $A'(\theta_0)$  is a tensor and  $A'(\theta_0) \in \mathbb{R}^{3n \times M \times 3n}$

---

**Algorithm 2:** Least-Squares Contact Force Optimization with Tip Position Constraint Under Surface Motion

---

**Input :**  $u^0, f_{cn}^d, \{\Psi(x_0, t_i), i = 1, \dots, m\}$

- 1  $j \leftarrow 0$
- 2 **repeat**
- 3   **for** all  $i$  in heart motion samples  $\{1, 2, \dots, m\}$
- 4     **do**
- 5        $\theta_i^j \leftarrow \text{constrained\_equilibrium}(u^j, \Psi(x_0, t_i))$
- 6        $J_i \leftarrow -J_C^T A(\theta_i^j)$
- 7        $f_{c_i} \leftarrow$   
       compute\\_contact\\_force( $\theta_i^j, u^j, \Psi(x_0, t_i)$ )
- 8        $df_{c_i}^n \leftarrow k_n(f_{cn}^d - f_{c_i}^n)$
- 9        $df_{c_i} \leftarrow (-k_f f_{c_i}^x, -k_f f_{c_i}^y, df_{c_i}^n)$
- 10     **end**
- 11    $J \leftarrow [J_1^T, J_2^T, \dots, J_m^T]^T$
- 12    $df_c \leftarrow [df_{c_1}^T, df_{c_2}^T, \dots, df_{c_m}^T]^T$
- 13    $du \leftarrow (J^T W_I J)^{-1} J^T W_I df_c$
- 14    $u^{j+1} \leftarrow u^j + du$
- 15    $j \leftarrow j + 1$
- 16 **until** ( $j = \text{IterationLimit}$ ) or ( $\|du\| < \epsilon$ );

**Output:**  $u^j$

---

## 5.2 Least-Squares Contact Force Optimization Algorithm

In the least-squares contact force optimization algorithm, the actuation currents are optimized to achieve the desired normal contact force over a control horizon for a given estimated heart motion trajectory. The proposed contact force optimization algorithm iteratively computes the actuation currents that best approximates the desired contact force over a given heart motion trajectory in a least-squares sense. The full least-squares contact force optimization algorithm is given in Algorithm 2.

The algorithm again assumes that the catheter tip is initially in contact with the target point on the tissue surface. The initial actuation current  $u^0$ , the desired normal contact force  $f_{cn}^d$ , and the spatial coordinates of the predicted positions of the contact point on the tissue surface  $\{\Psi(x_0, t_i), i = 1, \dots, m\}$  are given as inputs. First, the algorithm collects the contact force-actuation Jacobians and the calculated incremental changes of the contact forces for all of the tip positions throughout the estimated heart motion over the horizon. Specifically, for each tip position in the heart beat cycle  $i$ , the equilibrium joint angles  $\theta_i$  under catheter tip position constraint are obtained in Line 4. Similar to Algorithm 1, the contact force-actuation Jacobian is calculated and collected by  $J_i$  in Line 5. The incremental change of the contact force is calculated and collected by  $df_{c_i}$  in Lines 6-8.  $k_n$  is the step size to regulate the change of normal contact force, and a negative feedback  $-k_f$  is applied on the tangential forces to keep the contact force inside the friction cone. Lines 10-12 compute the actuation current update  $du$  as a weighted least-squares problem, where  $W_I$  is the weight matrix. The actuation currents are then updated in Line 13.

## 5.3 Contact Force Control Schemes Under Surface Motion

Based on the contact force optimization algorithms presented in Algorithm 1 and 2, we propose four contact force control schemes for achieving stable and safe catheter tip-tissue contact under heart surface motions as shown in Fig .3.

*Scheme 1:* In the first control scheme, the actuation currents obtained from the quasi-static contact force optimization algorithm presented in Algorithm 1 are updated at the servo control rate using the instantaneous point-of-interest (POI) position feedback of the catheter tip. This scheme is referred as instantaneous feedback contact force control (IFC) scheme in the rest of the paper.

*Scheme 2:* In this control scheme, a single actuation current set is optimized using the least-squares contact force optimization algorithm presented in Algorithm 2 given the first cycle of the heart motion, and is applied throughout the rest of the heart beat motions. This proposed control scheme assumes that the heart motion is quasi-periodic, where the first cycle of the heart motion data is used as the prediction of the heart motion for the subsequent heart beats, and identifies a constant actuation that optimizes the contact stability and safety. We refer to this control scheme as constant actuation level contact force control (CALC).

*Scheme 3:* In this control scheme, the actuation currents are calculated using Algorithm 1 at the predicted instantaneous POI position, accounting for the system latency caused by MRI image processing, heart motion estimation, and control calculations, etc.. The currents obtained are then updated at the servo control rate. The generalized adaptive filter based heart motion prediction proposed in [16] is used to provide the estimated instantaneous POI positions. This scheme is referred as prediction feedback contact force control (PFC) scheme.

*Scheme 4:* The last contact force control scheme employs a receding horizon control approach [15, 46]. The generalized adaptive filter based heart motion prediction is used to provide the estimated heart motion trajectory for the control horizon. The estimated trajectory is used to calculate actuation current values over the control horizon using the least-squares contact force optimization algorithm presented in Algorithm 2. The optimized control value corresponding to the system latency is then applied to the robotic catheter for actuation. The calculation is repeated at the servo control rate of the system with control horizon receding in time. We refer to this control scheme as receding horizon contact force control with adaptive filter based prediction (RHCAF).

## 6 Simulation-Based Validation Studies

### 6.1 Simulation Environment Setup

The parameters of catheter robot model used in this paper are based on the parameters identified in [47] of our MRI-actuated robotic catheter prototype. The mechanical model of the catheter has 5 pseudo-rigid links, each with 20 mm length, for a total catheter length of 100 mm. In this simulation study, a servo control sampling period of 48 ms, ap-

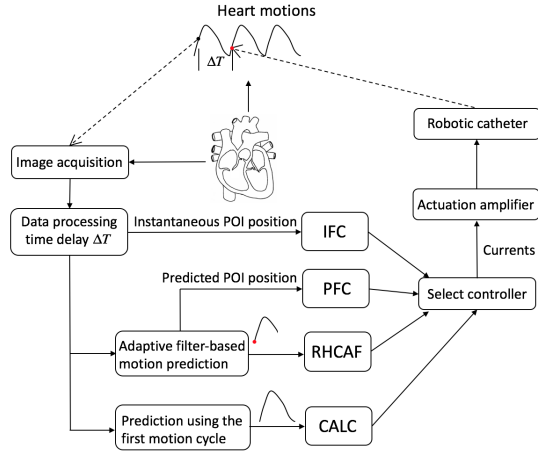


Fig. 3. Illustration of the four proposed contact force control schemes.  $\Delta T$  denotes the potential time lag caused by image acquisition. In IFC, each actuation output is computed at the instantaneous POI position and updated at servo control rate. In CALC, the actuation output is optimized over the first cycle of the heart motion and applied to the rest of the motion. In PFC, the actuation output is computed at the predicted position provided by the generalized adaptive filter and updated at servo control rate. In RHCAF, the actuation output is optimized over the estimated motion trajectory for the control horizon, and updated at servo control rate.

proximately matching the targeted servo control rate of 20 Hz of the prototype catheter system [48], is used. For evaluation of the control performance, we have used two types of *in vivo* heartbeat motion data combined with respiratory motion, as shown in Fig. 4. First, the regular heart motion data collected from a swine model in our earlier studies [16], is tested. Specifically, the data used is a 62.5 s long recording of the motion of a POI on the left ventricular (LV) of a free beating heart with uniform heart rate, sampled at a 249 Hz sampling rate. In addition, a 128 s long heart motion data with arrhythmia is used for evaluating the performance of the proposed schemes under the presence of arrhythmia motions [17]. The arrhythmia motion data is sampled at a 404.5 Hz sampling rate. The variance of the regular heart motion and the arrhythmia motion data are 6.97 mm and 3.48 mm, respectively.

Due to the processing time required for localization of the heart surface from MRI images, a time lag of  $\Delta T$  between the data acquisition from the MRI and the update of actuation currents is introduced, where the actuation currents are applied to the heart beat positions  $\Delta T$  after the measurement is acquired. Specifically,  $\Delta T = 75$  ms, 100 ms, 125 ms, 150 ms and 175 ms are evaluated with the proposed contact force control schemes over the given heart motions.

In the simulation studies, a normal contact force range from 0.10 N to 0.25 N is used based on the values reported in the earlier literature, as discussed in Section 2. A desired normal force of 0.15 N is used for the proposed contact force control schemes in order to leave enough tolerance between the desired force and the lower/upper force limits.

One of the key assumptions used in the formulation pre-

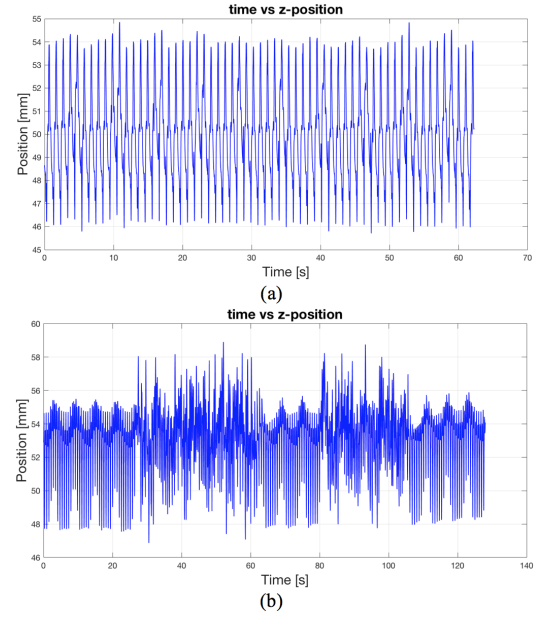


Fig. 4. (a) The z-axis position data of the 62.5 s long regular heart motion (cardiac and respiratory motion). (b) The z-axis position data of the 128 s long heart motion under the presence of arrhythmia.

sented in Section 5 is that the cardiac tissue surface is much stiffer than the catheter and hence the surface deformation can be ignored. In order to verify the validity of this assumption, the stiffness values of the catheter and the cardiac tissue were estimated and compared. Silicone rubber is used as the material for the body of the catheter prototype [10] (Fig. 1). The stiffness of the robotic catheter  $k_c$  is evaluated to be  $k_c = 0.23$  N/m at the configuration used in the validation studies under the normal contact force of 0.15 N. The stiffness of the heart tissue  $k_s$  is estimated using the equation provided in [49, 50] for surface stiffness observed by a cylindrical indenter on a flat surface, as  $k_s = 2ER/(1 - \nu^2) = 423.3$  N/m, where  $E = 100$  kPa is the Young's modulus and  $\nu \approx 0.5$  is the Poisson's ratio of the heart muscle, and  $R = 1.58$  mm is the outer radius of the catheter. As the estimated stiffness of the heart muscles is much greater than the stiffness of the robotic catheter ( $k_s \gg k_c$ ), a stiff contact between the catheter tip and the heart tissue surface is a valid approximation.

The internal wall of the heart is relatively smooth and well-lubricated due to the presence of blood [51]. The static friction coefficient between the catheter tip and blood vessel depends on the material of the catheter and the type of lubricant used [52, 53]. In [52], the static friction coefficient of a silicone catheter against porcine aorta is reported as 0.1, where distilled water is used as lubricant. In [53], the static friction coefficients of a silicone catheter against aorta and superior vena cava are reported as 0.67 and 0.56, respectively, where blood is used as lubricant for both cases. In this study, we use a relatively conservative value of  $\mu_s = 0.2$  as the static friction coefficient between the robotic catheter and the atrial surface [11].

## 6.2 Control Schemes Setup

For the evaluation of the IFC and PFC schemes, a desired normal contact force value of  $f_{cn}^d = 0.15$  N is used. The obtained actuation currents are then applied to the catheter for the 48 ms sampling duration, until the next sample time, while the ‘actual’ contact forces and contact ratios are calculated at the full sampling rate of the underlying heart motion data. The adaptive filter based heart motion prediction used in the PFC (and RHCAF) scheme has a sampling period of 48 ms, matching the servo control rate, since there will be a single MRI-based estimation of the target tissue motion at every sample period. The PFC is performed after the first 2.4 s of the heart motion data, for the adaptive filter to converge. The resulting contact ratio and normal contact force over the remaining heart motion data are calculated for evaluation of the proposed schemes.

In the CALC scheme, the desired normal contact force is given as  $f_{cn}^d = 0.15$  N for the least-squares contact force optimization algorithm, with the update rates  $k_n = 0.003$  and  $k_f = 0.005$  for the normal and tangential forces, respectively. The CALC scheme assumes the heart motion is periodic and uses one set of optimized actuation currents throughout the full heart motion, thus the resulting contact ratio and normal contact force is not affected by time lag  $\Delta T$ .

Finally, for the validation of the RHCAF scheme, similar to the other schemes, the desired normal contact force of  $f_{cn}^d = 0.15$  N is used. The least-squares contact force optimization is performed using the estimated heart motion data. The obtained actuation currents are then applied to the real heart motion data and updated at servo control rate. Similar to the PFC scheme, the RHCAF is performed after the first 2.4 s of the heart motion data, for full convergence of the adaptive filter. The resulting contact ratio and normal contact force are calculated for the remaining heart motion data.

## 6.3 Simulation Results

In this section, the results of the simulation-based validation studies evaluating the performance of the proposed contact force control schemes are presented. First, the simulation results of contact ratio and normal contact force over the full 62.5 seconds of regular heart motions are summarized in Table 1.

As shown in Table 1, all of the proposed contact force control schemes achieved the average normal force of 0.15 N, the desired normal contact force, for all of the time lag values considered, with no violations of the force limits detected. In the CALC scheme, 9.8% of heart motion samples can cause potential slippage between the catheter tip and tissue surface during the given heart motions, with maximum contact ratio of 0.23. In the IFC scheme, when no time lag is considered, 1.4% of the heart motion samples violated the friction coefficient, with maximum contact ratio of 0.21. However, the number of heart position samples that violated the friction coefficient increased drastically as the time lag increased. At  $\Delta T = 175$  ms, 13.7% of the motion samples violated the friction coefficient, with maximum contact ratio of 0.25. In contrast, the PFC scheme is able to provide

better contact stability with 4.1% of sample violations of the friction coefficient at  $\Delta T = 175$  ms. The RHCAF scheme outperforms the other schemes in terms of contact stability for all the given time lags, with 3.9% of the motion samples violating the force limits at  $\Delta T = 175$  ms. No loss of contact is detected during the regular heart motion using the four proposed control schemes.

Table 2 presents the simulation results of the contact ratio and normal force of the 128 s long heartbeat motion under the presence of arrhythmia. All four proposed control schemes achieved the average normal force of 0.15 N, with no violation of the force limits. The RHCAF scheme is able to provide better contact stability, compared to IFC and PFC scheme, with maximum of 2.2% motion samples violated the friction coefficient for time lag  $\Delta T = 175$  ms. When no time lag is considered, compared to the CALC scheme, the RHCAF scheme is able to provide better catheter-tissue contact stability with 1.7 % violations of friction coefficient. However, as time lag increases, the CALC scheme outperforms the other proposed control schemes, with 1.9 % violations of the friction coefficient. No loss of contact is detected during the heartbeat motion under arrhythmia for all control schemes.

Finally, the simulation results of contact stability and contact safety achieved without employing any control scheme are provided in Table 3 as baseline performances. As shown in Table 3, 5 different motion positions sampled from the first heart motion cycle are selected, where at each of the sampled positions, a single actuation current set is obtained with normal force of 0.15 N (the desired normal force used for the proposed control schemes) and applied throughout the rest of heartbeat motions.

The results in Table 3 show that, for both regular and arrhythmia heartbeat motions, without a specific control scheme, the robotic catheter cannot guarantee to achieve the desired average normal force value. Furthermore, in the no control scheme case, the quality of the contact, in terms of the contact stability and mean contact force, is highly dependent on the time point in the heart cycle where the control is applied. In contrast to the baseline performance, both PFC scheme and RHCAF scheme show great improvement on contact stability for the regular heart motions with desired normal contact force achieved. In the case of heartbeat motions under arrhythmia, the proposed PFC, RHCAF and CALC schemes are able to provide better catheter-tissue contact stability while sustaining the desired normal contact force, as the time lag  $\Delta T$  increases.

## 7 Discussion

The simulation based study provides an evaluation of the proposed contact force control schemes on achieving contact stability and contact safety given heart motion disturbances, which paves the way for hardware implementation and validation of the proposed contact force control methods in future research. The validation of the kinematic model and the contact model of the robotic catheter employed in this paper were performed in [40,43,45,54,55]. Specifically, the valida-

Table 1. Performance of the proposed control schemes under regular heart motion: experimental results of mean, max values of contact ratio  $\sigma_\mu$ , percentage of the regular heart motion samples that violated the friction coefficient, and min, mean, max values of normal contact force  $f_{cn}$ , given different time lags between the measurement acquisition and actuation update. The CALC scheme assumes the heart motion is periodic and uses one optimized actuation currents throughout the full heart motion, thus the resulting contact ratio and normal contact force is not affected by time lags

| Control Schemes | Metrics      | Time Lag (ms)     |                  |                  |                  |                  |                  |                  |
|-----------------|--------------|-------------------|------------------|------------------|------------------|------------------|------------------|------------------|
|                 |              | 0                 | 75               | 100              | 125              | 150              | 175              |                  |
| IFC scheme      | $\sigma_\mu$ | Mean (Max)        | 0.14 (0.21)      | 0.14 (0.22)      | 0.14 (0.22)      | 0.14 (0.23)      | 0.14 (0.24)      | 0.15 (0.25)      |
|                 |              | Violations[%]     | 1.4              | 3.3              | 4.4              | 7.7              | 11.1             | 13.7             |
|                 | $f_{cn}$     | Mean[N] (Min/Max) | 0.15 (0.13/0.17) | 0.15 (0.13/0.18) | 0.15 (0.13/0.18) | 0.15 (0.13/0.18) | 0.15 (0.13/0.19) | 0.15 (0.13/0.19) |
| PFC scheme      | $\sigma_\mu$ | Mean (Max)        | 0.13 (0.21)      | 0.13 (0.22)      | 0.13 (0.22)      | 0.14 (0.22)      | 0.13 (0.22)      | 0.13 (0.23)      |
|                 |              | Violations[%]     | 1.4              | 2.8              | 3.3              | 3.8              | 3.9              | 4.1              |
|                 | $f_{cn}$     | Mean[N] (Min/Max) | 0.15 (0.13/0.17) | 0.15 (0.13/0.17) | 0.15 (0.13/0.17) | 0.15 (0.13/0.17) | 0.15 (0.13/0.17) | 0.15 (0.13/0.17) |
| RHCAF scheme    | $\sigma_\mu$ | Mean (Max)        | 0.13 (0.21)      | 0.13 (0.22)      | 0.13 (0.22)      | 0.13 (0.22)      | 0.13 (0.22)      | 0.13 (0.23)      |
|                 |              | Violations[%]     | 1.2              | 2.7              | 3.2              | 3.7              | 3.7              | 3.9              |
|                 | $f_{cn}$     | Mean[N] (Min/Max) | 0.15 (0.13/0.18) | 0.15 (0.13/0.17) | 0.15 (0.13/0.18) | 0.15 (0.13/0.18) | 0.15 (0.13/0.18) | 0.15 (0.13/0.18) |
| CALC scheme     | $\sigma_\mu$ | Mean (Max)        | 0.14 (0.23)      |                  |                  |                  |                  |                  |
|                 |              | Violations[%]     | 9.8              |                  |                  |                  |                  |                  |
|                 | $f_{cn}$     | Mean[N] (Min/Max) | 0.15 (0.13/0.16) |                  |                  |                  |                  |                  |

tion of pseudo-rigid-body model of the MRI-actuated robotic catheter can be found in [40, 43], and the contact model used in this paper is verified in [45, 54, 55].

The presented simulation results indicate that the proposed contact force control schemes are able to improve the contact stability while maintaining the safety of the normal contact force. Due to the lack of prediction, the IFC scheme cannot accommodate large time lags between the measurement acquisition and current update, and fails to provide stable and safe catheter-tissue contact as the time lag increases. On the other hand, the prediction based contact force control schemes (PFC, RHCAF, CALC) are able to compensate for the potential time lags and optimize the actuation currents using the estimated heart motion trajectories over the future horizon, achieving safer and more stable contact forces when dealing with the rapidly changing heart motions. The performance of the CALC scheme on the arrhythmia motion is significantly better than its performance on the regular motion. This is due to the larger magnitude of the regular heart motion, which is almost twice as large as the magnitude of the arrhythmia motion. The CALC scheme outperforms the RHCAF scheme for the arrhythmia heartbeat motions when time lag  $\Delta T > 75$  ms. One of the major reasons is that the prediction error of the employed generalized adaptive filter based heart motion predictor tends to increase as the prediction horizon increases.

While the simulation results demonstrate the feasibility

of the proposed contact force control schemes, several limitations of the proposed methods are identified. In this work, the robotic catheter is modeled by the pseudo-rigid-body model, which cannot guarantee the smoothness of the catheter shape, for computation efficiency and proof-of-concept. This can be improved by employing the continuum model proposed in [10]. Avoiding ill-conditioned contact force-actuation Jacobian is also important for the proposed contact force control methods. In this study, both quasi-static and least-squares based contact force optimization algorithms need to start in a stable configuration in order to avoid abrupt changes in contact force. Since this paper emphasizes on the contact stability and safety under the effect of the positional heart motions, the change of the surface orientation during the heart beat motion is ignored in the simulation experiments. A potential avenue for future work is to include the angle between the catheter tip and the tissue surface normal as an additional optimization objective.

The proposed algorithms were implemented in MATLAB<sup>®</sup> (R2019a) on Ubuntu 16.04 operating system. The computer is equipped with Intel<sup>®</sup> Core<sup>™</sup> i7-8700 CPU @ 3.20 GHz and 8.0 GB memory. MATLAB's constrained optimization function *fmincon* is employed for computing the constrained equilibrium configuration of the robotic catheter, using the default 'interior-point' algorithm with a linear equality constraint and a linear inequality constraint for satisfying the desired tip position constraint on the tissue surface.

Table 2. Performance of the proposed control schemes under arrhythmia heart motion: experimental results of mean, max values of contact ratio  $\sigma_\mu$ , percentage of the heart motion samples under arrhythmia that violated the friction coefficient, and min, mean, max values of normal contact force  $f_{cn}$ , given different time lags between the measurement acquisition and actuation update

| Control Schemes | Metrics      | Time Lag (ms)     |                  |                  |                  |                  |                  |                  |
|-----------------|--------------|-------------------|------------------|------------------|------------------|------------------|------------------|------------------|
|                 |              | 0                 | 75               | 100              | 125              | 150              | 175              |                  |
| IFC scheme      | $\sigma_\mu$ | Mean (Max)        | 0.14 (0.25)      | 0.15 (0.26)      | 0.15 (0.26)      | 0.15 (0.26)      | 0.15 (0.26)      | 0.15 (0.25)      |
|                 |              | Violations[%]     | 1.9              | 4.6              | 6.3              | 7.5              | 7.7              | 7.0              |
|                 | $f_{cn}$     | Mean[N] (Min/Max) | 0.15 (0.13/0.19) | 0.15 (0.12/0.19) | 0.15 (0.11/0.19) | 0.15 (0.11/0.19) | 0.15 (0.11/0.18) | 0.15 (0.11/0.18) |
| PFC scheme      | $\sigma_\mu$ | Mean (Max)        | 0.14 (0.25)      | 0.14 (0.26)      | 0.14 (0.25)      | 0.14 (0.25)      | 0.14 (0.25)      | 0.14 (0.25)      |
|                 |              | Violations[%]     | 1.9              | 2.3              | 2.3              | 2.4              | 2.4              | 2.4              |
|                 | $f_{cn}$     | Mean[N] (Min/Max) | 0.15 (0.12/0.18) | 0.15 (0.13/0.18) | 0.15 (0.13/0.18) | 0.15 (0.13/0.17) | 0.15 (0.13/0.17) | 0.15 (0.13/0.18) |
| RHCAF scheme    | $\sigma_\mu$ | Mean (Max)        | 0.14 (0.25)      | 0.14 (0.25)      | 0.14 (0.26)      | 0.14 (0.25)      | 0.14 (0.25)      | 0.14 (0.25)      |
|                 |              | Violations[%]     | 1.7              | 2.0              | 2.1              | 2.2              | 2.2              | 2.2              |
|                 | $f_{cn}$     | Mean[N] (Min/Max) | 0.15 (0.13/0.18) | 0.15 (0.12/0.18) | 0.15 (0.12/0.18) | 0.15 (0.12/0.18) | 0.15 (0.13/0.18) | 0.15 (0.13/0.18) |
| CALC scheme     | $\sigma_\mu$ | Mean (Max)        | 0.13 (0.24)      |                  |                  |                  |                  |                  |
|                 |              | Violations[%]     | 1.9              |                  |                  |                  |                  |                  |
|                 | $f_{cn}$     | Mean[N] (Min/Max) | 0.15 (0.13/0.17) |                  |                  |                  |                  |                  |

Table 3. Baseline performance obtained without employing any control schemes: experimental results of mean, max values of contact ratio  $\sigma_\mu$ , percentage of the motion samples that violated the friction coefficient, and min, mean, max values of normal contact force  $f_{cn}$ , for actuation currents obtained at different positions during the first motion cycle.

| Motion Types      | Metrics      | Sampled Positions |                  |                  |                  |                  |                  |
|-------------------|--------------|-------------------|------------------|------------------|------------------|------------------|------------------|
|                   |              | 1                 | 2                | 3                | 4                | 5                |                  |
| Regular Motion    | $\sigma_\mu$ | Mean (Max)        | 0.16 (0.27)      | 0.14 (0.25)      | 0.13 (0.22)      | 0.15 (0.24)      | 0.16 (0.28)      |
|                   |              | Violations[%]     | 18.6             | 12.3             | 6.5              | 17.8             | 19.7             |
|                   | $f_{cn}$     | Mean[N] (Min/Max) | 0.16 (0.14/0.18) | 0.15 (0.13/0.17) | 0.14 (0.12/0.16) | 0.15 (0.13/0.17) | 0.16 (0.14/0.18) |
| Arrhythmia Motion | $\sigma_\mu$ | Mean (Max)        | 0.15 (0.25)      | 0.16 (0.25)      | 0.14 (0.25)      | 0.14 (0.26)      | 0.15 (0.26)      |
|                   |              | Violations[%]     | 4.3              | 9.7              | 2.4              | 4.8              | 4.9              |
|                   | $f_{cn}$     | Mean[N] (Min/Max) | 0.15 (0.13/0.17) | 0.16 (0.13/0.18) | 0.15 (0.13/0.17) | 0.14 (0.12/0.16) | 0.15 (0.12/0.17) |

In the quasi-static contact force optimization algorithm, the computation time of computing one iteration of the actuation update is approximately 40 ms. For least-squares contact force optimization, the computation time of one iteration of the current update for one predicted horizon is approximately 650 ms. The computation time for the least-squares contact force optimization algorithm can be significantly improved by parallelization of solving the constrained equilibrium and the Jacobian computations for the heart beat motions over the expected horizon. The computation time of the algorithms can be further improved by a computationally efficient C/C++ implementation.

Our future work will focus on the hardware implementation and validation of the proposed contact force control

schemes. The experimental validation of the proposed methods on hardware will be performed once the algorithms for real-time tracking of the robotic catheter system and the tissue surface from intra-operative MRI imaging are available. These algorithms are currently under development as part of a parallel research study in our research group. Our future work will also focus on the improvement of the computation efficiency of the proposed algorithms, specifically, the parallel computing based implementation of the least-squares contact force optimization.

## 8 Conclusions

In this paper, the contact stability and contact safety of a novel magnetically-actuated robotic catheter under regular and arrhythmia heart motions are studied. A catheter-tissue contact model based on Pseudo-Rigid-Body Model of the robotic catheter is presented, and the contact force-actuation Jacobian is formulated. Two contact force optimization methods are proposed. The first method is a quasi-static contact force optimization algorithm which improves the contact stability and safety given an instantaneous surface configuration. Two contact force control schemes, an instantaneous heart position feedback and a predicted position feedback based contact force control scheme, are proposed based on this algorithm. The second optimization method is a least-squares contact force optimization algorithm which optimizes the actuation currents for the estimated heart motions over a control horizon. A receding horizon control scheme with an adaptive filter based heart motion prediction and a constant actuation level contact force control scheme are proposed based on this optimization method.

The simulation-based validations are presented for evaluating the performance of the proposed contact force control schemes. The simulation results show that the contact force control schemes proposed based on least-squares contact force optimization algorithm are able to provide the most stable and safe contact force between the catheter tip and tissue surface under heart motions and sensing-to-actuation time delays.

## References

- [1] Kanagaratnam, P., Koa-Wing, M., Wallace, D. T., Goldenberg, A. S., Peters, N. S., and Davies, D. W., 2008. "Experience of robotic catheter ablation in humans using a novel remotely steerable catheter sheath". *Journal of Interventional Cardiac Electrophysiology*, **21**(1), pp. 19–26.
- [2] Kesner, S. B., and Howe, R. D., 2011. "Position control of motion compensation cardiac catheters". *IEEE Transactions on Robotics*, **27**(6), pp. 1045–1055.
- [3] Saliba, W., Reddy, V. Y., Wazni, O., Cummings, J. E., Burkhardt, J. D., Haissaguerre, M., Kautzner, J., Peichl, P., Neuzil, P., Schibgilla, V., et al., 2008. "Atrial fibrillation ablation using a robotic catheter remote control system: initial human experience and long-term follow-up results". *Journal of the American College of Cardiology*, **51**(25), pp. 2407–2411.
- [4] Kesner, S. B., and Howe, R. D., 2014. "Robotic catheter cardiac ablation combining ultrasound guidance and force control". *The International Journal of Robotics Research*, **33**(4), pp. 631–644.
- [5] Friedman, P. A., 2012. "Hitting a moving target: Catheter ablation and respiration". *Heart rhythm*, **9**(7), pp. 1048–1049.
- [6] Kuck, K.-H., Reddy, V. Y., Schmidt, B., Natale, A., Neuzil, P., Saoudi, N., Kautzner, J., Herrera, C., Hindricks, G., Jais, P., et al., 2012. "A novel radiofrequency ablation catheter using contact force sensing: Toccata study". *Heart rhythm*, **9**(1), pp. 18–23.
- [7] Ariyaratna, N., Kumar, S., Thomas, S. P., Stevenson, W. G., and Michaud, G. F., 2018. "Role of contact force sensing in catheter ablation of cardiac arrhythmias: evolution or history repeating itself?". *JACC: Clinical Electrophysiology*, **4**(6), pp. 707–723.
- [8] Makimoto, H., Lin, T., Rillig, A., Metzner, A., Wohlmuth, P., Arya, A., Antz, M., Mathew, S., Deiss, S., Wissner, E., et al., 2014. "In vivo contact force analysis and correlation with tissue impedance during left atrial mapping and catheter ablation of atrial fibrillation". *Circulation: Arrhythmia and Electrophysiology*, **7**(1), pp. 46–54.
- [9] Greigarn, T., 2018. "Kinematics, planning, and perception for magnetically-actuated mri-guided continuum robots". PhD thesis, Case Western Reserve University.
- [10] Liu, T., Poirot, N. L., Franson, D., Seiberlich, N., Griswold, M. A., and Cavusoglu, M. C., 2016. "Modeling and validation of the three-dimensional deflection of an MRI-compatible magnetically actuated steerable catheter". *IEEE Trans. Biomed. Engineering*, **63**(10), pp. 2142–2154.
- [11] Liu, T., Poirot, N., Greigarn, T., and Cavusoglu, M., 2017. "Design of an MRI-guided magnetically-actuated steerable catheter". *ASME Journal of Medical Devices, Special Issue on Cardiovascular Device Development and Safety Assessment using Computational and/or Experimental Approaches*, **11**.
- [12] Roberts, T., Hassenzahl, W., Hetts, S., and Arenson, R., 2002. "Remote control of catheter tip deflection: an opportunity for interventional MRI". *Magnetic Resonance in Medicine: An Official Journal of the International Society for Magnetic Resonance in Medicine*, **48**(6), pp. 1091–1095.
- [13] Gudino, N., Heilman, J., Derakhshan, J., Sunshine, J., Duerk, J., and Griswold, M., 2011. "Control of intravascular catheters using an array of active steering coils". *Medical Physics*, **38**(7), pp. 4215–4224.
- [14] Liu, T., and Çavuşoğlu, M. C., 2014. "Three dimensional modeling of an mri actuated steerable catheter system". In 2014 IEEE international conference on robotics and automation (ICRA), IEEE, pp. 4393–4398.
- [15] Bebek, O., and Çavuşoğlu, M. C., 2007. "Intelligent control algorithms for robotic-assisted beating heart surgery". *IEEE Transactions on Robotics*, **23**(3), pp. 468–480.
- [16] Tuna, E. E., Franke, T. J., Bebek, O., Shiose, A., Fukamachi, K., and Cavusoglu, M. C., 2012. "Heart motion prediction based on adaptive estimation algorithms for robotic-assisted beating heart surgery". *IEEE Transactions on Robotics*, **29**(1), pp. 261–276.
- [17] Tuna, E. E., H., K. J., Liu, T., Bebek, O., Fukamachi, K., and Çavuşoğlu, M. C., 2014. "Towards active tracking of beating heart motion in the presence of arrhythmia for robotic assisted beating heart surgery". *PLoS One*, **9**(7), p. e102877.

- [18] Pedrote, A., Acosta, J., Jauregui-Garrido, B., Frutos-Lopez, M., and Arana-Rueda, E., 2017. “Paroxysmal atrial fibrillation ablation: Achieving permanent pulmonary vein isolation by point-by-point radiofrequency lesions”. *World journal of cardiology*, **9**(3), p. 230.
- [19] Williams, S. E., Harrison, J., Chubb, H., Bloch, L. Ø., Andersen, N. P., Dam, H., Karim, R., Whitaker, J., Gill, J., Cooklin, M., et al., 2015. “The effect of contact force in atrial radiofrequency ablation: electroanatomical, cardiovascular magnetic resonance, and histological assessment in a chronic porcine model”. *JACC: Clinical Electrophysiology*, **1**(5), pp. 421–431.
- [20] Reddy, V. Y., Shah, D., Kautzner, J., Schmidt, B., Saoudi, N., Herrera, C., Jais, P., Hindricks, G., Peichl, P., Yulzari, A., et al., 2012. “The relationship between contact force and clinical outcome during radiofrequency catheter ablation of atrial fibrillation in the toccata study”. *Heart rhythm*, **9**(11), pp. 1789–1795.
- [21] Thiagalingam, A., D’AVILA, A., Foley, L., Guerrero, J. L., Lambert, H., Leo, G., Ruskin, J. N., and Reddy, V. Y., 2010. “Importance of catheter contact force during irrigated radiofrequency ablation: evaluation in a porcine ex vivo model using a force-sensing catheter”. *Journal of cardiovascular electrophysiology*, **21**(7), pp. 806–811.
- [22] Wakili, R., Clauss, S., Schmidt, V., Ulbrich, M., Hahnefeld, A., Schüssler, F., Siebermair, J., Kääb, S., and Estner, H. L., 2014. “Impact of real-time contact force and impedance measurement in pulmonary vein isolation procedures for treatment of atrial fibrillation”. *Clinical Research in Cardiology*, **103**(2), pp. 97–106.
- [23] Di Biase, L., Natale, A., Barrett, C., Tan, C., Elayi, C. S., Ching, C. K., Wang, P., AL-AHMAD, A., Arruda, M., Burkhardt, J. D., et al., 2009. “Relationship between catheter forces, lesion characteristics, “popping,” and char formation: experience with robotic navigation system”. *Journal of cardiovascular electrophysiology*, **20**(4), pp. 436–440.
- [24] Andrade, J. G., Monir, G., Pollak, S. J., Khairy, P., Dubuc, M., Roy, D., Talajic, M., Deyell, M., Rivard, L., Thibault, B., et al., 2014. “Pulmonary vein isolation using “contact force” ablation: the effect on dormant conduction and long-term freedom from recurrent atrial fibrillation—a prospective study”. *Heart Rhythm*, **11**(11), pp. 1919–1924.
- [25] Dewire, J., and Calkins, H., 2013. “Update on atrial fibrillation catheter ablation technologies and techniques”. *Nature Reviews Cardiology*, **10**(10), p. 599.
- [26] Di Biase, L., Wang, Y., Horton, R., Gallinghouse, G. J., Mohanty, P., Sanchez, J., Patel, D., Dare, M., Canby, R., Price, L. D., et al., 2009. “Ablation of atrial fibrillation utilizing robotic catheter navigation in comparison to manual navigation and ablation: Single-center experience”. *Journal of cardiovascular electrophysiology*, **20**(12), pp. 1328–1335.
- [27] Jayender, J., Azizian, M., and Patel, R. V., 2008. “Autonomous image-guided robot-assisted active catheter insertion”. *IEEE Transactions on Robotics*, **24**(4), pp. 858–871.
- [28] Srimathveeravalli, G., Kesavadas, T., and Li, X., 2010. “Design and fabrication of a robotic mechanism for remote steering and positioning of interventional devices”. *The International Journal of Medical Robotics and Computer Assisted Surgery*, **6**(2), pp. 160–170.
- [29] Yuen, S. G., Yip, M. C., Vasilyev, N. V., Perrin, D. P., Pedro, J., and Howe, R. D., 2009. “Robotic force stabilization for beating heart intracardiac surgery”. In *International Conference on Medical Image Computing and Computer-Assisted Intervention*, Springer, pp. 26–33.
- [30] Yip, M. C., Sganga, J. A., and Camarillo, D. B., 2017. “Autonomous control of continuum robot manipulators for complex cardiac ablation tasks”. *Journal of Medical Robotics Research*, **2**(01), p. 1750002.
- [31] Khoshnam, M., Skanes, A. C., and Patel, R. V., 2015. “Modeling and estimation of tip contact force for steerable ablation catheters”. *IEEE Transactions on Biomedical Engineering*, **62**(5), pp. 1404–1415.
- [32] Hasanzadeh, S., and Janabi-Sharifi, F., 2015. “Model-based force estimation for intracardiac catheters”. *IEEE/ASME Transactions on Mechatronics*, **21**(1), pp. 154–162.
- [33] Back, J., Manwell, T., Karim, R., Rhode, K., Althoefer, K., and Liu, H., 2015. “Catheter contact force estimation from shape detection using a real-time cosserat rod model”. In *2015 IEEE/RSJ International Conference on Intelligent Robots and Systems (IROS)*, IEEE, pp. 2037–2042.
- [34] Razban, M., Dargahi, J., and Boulet, B., 2018. “A sensor-less catheter contact force estimation approach in endovascular intervention procedures”. In *2018 IEEE/RSJ International Conference on Intelligent Robots and Systems (IROS)*, IEEE, pp. 2100–2106.
- [35] Zhang, Z., Dequidt, J., Back, J., Liu, H., and Duriez, C., 2019. “Motion control of cable-driven continuum catheter robot through contacts”. *IEEE Robotics and Automation Letters*, **4**(2), pp. 1852–1859.
- [36] Haouchine, N., Kuang, W., Cotin, S., and Yip, M., 2018. “Vision-based force feedback estimation for robot-assisted surgery using instrument-constrained biomechanical three-dimensional maps”. *IEEE Robotics and Automation Letters*, **3**(3), pp. 2160–2165.
- [37] Hao, R., Greigarn, T., and Çavuşoğlu, M. C., 2020. “Contact stability analysis of magnetically-actuated robotic catheter under surface motion”. In *2020 IEEE International Conference on Robotics and Automation (ICRA)*, IEEE, pp. 4455–4462.
- [38] Greigarn, T., and Çavuşoğlu, M. C., 2015. “Pseudo-rigid-body model and kinematic analysis of MRI-actuated catheters”. In *IEEE International Conference on Robotics and Automation (ICRA)*, IEEE, pp. 2236–2243.
- [39] Liu, T., Jackson, R., Franson, D., Poirot, N. L., Criss, R. K., Seiberlich, N., Griswold, M. A., and Çavuşoğlu,

- M. C., 2017. “Iterative jacobian-based inverse kinematics and open-loop control of an MRI-guided magnetically actuated steerable catheter system”. *IEEE/ASME Transactions on Mechatronics*, **22**(4), pp. 1765–1776.
- [40] Greigarn, T., Jackson, R., Liu, T., and Çavuşoğlu, M. C., 2017. “Experimental validation of the pseudo-rigid-body model of the MRI-actuated catheter”. In IEEE International Conference on Robotics and Automation (ICRA), IEEE, pp. 3600–3605.
- [41] Khoshnam, M., and Patel, R. V., 2013. “A pseudo-rigid-body 3r model for a steerable ablation catheter”. In 2013 IEEE International Conference on Robotics and Automation, IEEE, pp. 4427–4432.
- [42] Su, H.-J., 2009. “A pseudorigid-body 3r model for determining large deflection of cantilever beams subject to tip loads”. *Journal of Mechanisms and Robotics*, **1**(2), p. 021008.
- [43] Greigarn, T., Poirot, N. L., Xu, X., and Cavusoglu, M. C., 2018. “Jacobian-based task-space motion planning for MRI-actuated continuum robots”. *IEEE Robotics and Automation Letters*.
- [44] Greigarn, T., and Çavuşoğlu, M. C., 2014. “Task-space motion planning of MRI-actuated catheters for catheter ablation of atrial fibrillation”. In IEEE International Conference on Intelligent Robots and Systems (IROS), IEEE, pp. 3476–3482.
- [45] Murray, R. M., 2017. *A mathematical introduction to robotic manipulation*. CRC press.
- [46] Mattingley, J., Wang, Y., and Boyd, S., 2011. “Receding horizon control”. *IEEE Control Systems Magazine*, **31**(3), pp. 52–65.
- [47] Greigarn, T., Liu, T., and Çavuşoğlu, M. C., 2016. “Parameter optimization of pseudo-rigid-body models of MRI-actuated catheters”. In Engineering in Medicine and Biology Society (EMBC), 2016 IEEE 38th Annual International Conference of the, IEEE, pp. 5112–5115.
- [48] Tuna, E. E., Liu, T., Jackson, R., Poirot, N. L., Russell, M., and Çavuşoğlu, M. C., 2018. “Analysis of dynamic response of an MRI-guided magnetically-actuated steerable catheter system”. In Proceedings of the IEEE/RSJ International Conference on Intelligent Robots and Systems (IROS), pp. 4927–4934.
- [49] Zhang, M., Zheng, Y., and Mak, A. F., 1997. “Estimating the effective young’s modulus of soft tissues from indentation tests—nonlinear finite element analysis of effects of friction and large deformation”. *Medical engineering & physics*, **19**(6), pp. 512–517.
- [50] McKee, C. T., Last, J. A., Russell, P., and Murphy, C. J., 2011. “Indentation versus tensile measurements of young’s modulus for soft biological tissues”. *Tissue Engineering Part B: Reviews*, **17**(3), pp. 155–164.
- [51] Ho, S. Y., Cabrera, J. A., and Sanchez-Quintana, D., 2012. “Left atrial anatomy revisited”. *Circulation: Arrhythmia and Electrophysiology*, **5**(1), pp. 220–228.
- [52] Kazmierska, K., Szwast, M., and Ciach, T., 2008. “Determination of urethral catheter surface lubricity”. *Journal of Materials Science: Materials in Medicine*, **19**(6), pp. 2301–2306.
- [53] Prokopovich, P., Perni, S., Piccirillo, C., Pratten, J., Parkin, I. P., and Wilson, M., 2010. “Frictional properties of light-activated antimicrobial polymers in blood vessels”. *Journal of Materials Science: Materials in Medicine*, **21**(2), pp. 815–821.
- [54] Lee, Y., Hwang, S., and Park, J., 2016. “Balancing of humanoid robot using contact force/moment control by task-oriented whole body control framework”. *Autonomous Robots*, **40**(3), pp. 457–472.
- [55] Magrini, E., Flacco, F., and De Luca, A., 2014. “Estimation of contact forces using a virtual force sensor”. In 2014 IEEE/RSJ International Conference on Intelligent Robots and Systems, IEEE, pp. 2126–2133.